IEEE Access
Multidisciplinary | Rapid Review | Open Access Journal

Received July 3, 2019, accepted July 24, 2019, date of publication July 26, 2019, date of current version August 13, 2019.

Digital Object Identifier 10.1109/ACCESS.2019.2931442

A Novel Rate-Control for Predictive Image Coding With Constant Quality

JOAN BARTRINA-RAPESTA[1], MICHAEL W. MARCELLIN[2], (Fellow, IEEE), JOAN SERRA-SAGRISTÁ[1], (Senior Member, IEEE), AND MIGUEL HERNÀNDEZ-CABRONERO[1]

[1]Department of Information and Communications Engineering, Universitat Autònoma de Barcelona, 08193 Barcelona, Spain
[2]Department of Electrical and Computing Engineering, University of Arizona, Tucson, AZ 85721-0104, USA

Corresponding author: Joan Bartrina-Rapesta (joan.bartrina@uab.cat)

This work was supported in part by the Spanish Ministry of Science, Innovation, and Universities (MICIU), in part by the European Regional Development Fund (FEDER) under Grant RTI2018-095287-B-I00, in part by the Catalan Government under Grant 2017SGR-463, and in part by the Centre National d'Études Spatiales (CNES).

ABSTRACT Predictive image coding systems yield a high-compression performance at low computational complexity, and are therefore popular in standards and prominent coding techniques for both lossless and near-lossless compression. However, few prediction-based coding techniques include rate-control approaches because of the difficulty in properly combining the prediction feedback loop and the quantization. None of the rate-control approaches for predictive image coding are focused on delivering homogeneous quality along the whole image. The main objective of this paper is to define a novel rate-control approach based on prediction that homogenises the quality over the entire image. The extensive experimental results, on medical, remote sensing, and natural images, suggest that our proposal attains more regular image quality and lower peak absolute error than the state-of-the-art approaches based on prediction and also transform-based techniques such as JPEG2000 and CCSDS-122.

INDEX TERMS Prediction-based image coding, rate-control, constant-quality lossy compression.

I. INTRODUCTION

The vast amount of digital image data generated for terrain analysis, military surveillance, personal use and other applications make compression techniques crucial for saving storage space and transmission time. Compression techniques can be classified into transform- and prediction-based. Both techniques have been employed in the last decade in image compression standards and prominent coding techniques.

Regarding prediction-based coding standards for lossless image compression, JPEG-LS [1], proposed by the Joint Photographic Experts Group [2], was the first standard devised principally for lossless compression of continous tone images. Its use within the medical community is widespread because it is included in the DICOM standard [3]. CCSDS-123.0-B-1 [4] is a recent standard designed for predictive coding of multi- and hyper-spectral scenes defined by the Multispectral & Hyperspectral Data Compression Working Group of the Consultative Committee for Space Data Systems (CCSDS) [5] (from now on, we refer to CCSDS-123.0-B-1 as CCSDS-123).

Predictive techniques are common for lossless, near-lossless and also for lossy compression, as witnessed by the large amount of publications in the literature [6]–[20]. Predictive lossless coding utilizes a causal predictor based on the original data followed by entropy coding of prediction residuals, often yielding high compression ratios [6]–[10]. In predictive lossy and near-lossless coding, a similar architecture is normally employed, although recovered sample data are used to predict new samples [1], and prediction residuals are quantized prior to entropy coding [11]–[17]. A rate-control mechanism can be added to produce codestreams for a given bit budget [21].

The main problem of rate control methods in prediction-based coding systems is the intricate mathematical relation between the rate and the quantized prediction residuals. Motivated by this issue, three distinct rate control methods that model the rate depending on the quantization step were recently proposed [18]–[20]. All three contributions have been evaluated with coding systems based on CCSDS-123,

The associate editor coordinating the review of this manuscript and approving it for publication was Michele Nappi.

and the main difference among them is related to what type of quantization structure is employed: [18] quantizes the data on a block-by-block basis, [19] selects and applies the quantization step on a slice-by-slice basis, and [20] quantizes the data on a spectral-line-by-spectral-line basis –a spectral-line is a line (row) of pixels with all its co-registered bands–. Although these three contributions yield similar rate-distortion performance, the third one provides the best average performance. In that work, the first spectral-line is losslessly encoded, and the quantization steps for the remaining spectral-lines are adapted dynamically to fit the constrained rate. This dynamic adjustment may lead to applying significantly different quantization steps in consecutive spectral-lines, potentially introducing large differences in terms of quality in the decoded image. Similar artifacts can occur with [18] and [19], since different quantization steps can be applied at block or slice level to reach the constrained rate. This effect is clearly illustrated in Section V, where decoded images encoded with the rate control proposed in [20] are depicted, along with those from the scheme proposed here.

Our current work introduces a novel rate control method designed to obtain homogeneous reconstruction quality in all image regions. The new method is incorporated in our previous contribution [17], which introduced a lossless and near-lossless coding system based on the predictor of CCSDS-123 followed by a lightweight binary contextual arithmetic encoder. The inclusion of the proposed rate control into [17] brings forward an original lossy compressor based on prediction. The proposed rate control strategy is evaluated against the state of the art [20] using images of different nature and dynamic ranges from 8 to 16 bits.

The rest of the paper is structured as follows: Section II reviews the CCSDS-123 coding system, a technique for controlling the error in a coding system based on prediction, the arithmetic coder introduced in our previous contribution [17], and the problem of optimal rate control; Section III presents our rate control method; Section IV defines a new coding system that employs the new rate control; and Section V provides the experimental results and discussion. Finally, Section VI concludes this work.

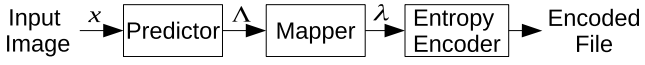

FIGURE 1. CCSDS-123 encoding scheme.

II. BACKGROUND

A. CCSDS-123

The purely lossless CCSDS-123 standard compressor is constituted by three stages: *Predictor*, *Mapper* and *Entropy Encoder*. Fig. 1 illustrates the encoding pipeline of CCSDS-123. CCSDS-123 encodes a digital image x (I columns, J rows, and K bands). The predictor estimates the value of the current sample $x_{i,j,k}$ using previously scanned samples. This predicted sample is denoted by $\widetilde{x}_{i,j,k}$. The prediction residual (error) Λ is computed as

$$\Lambda_{i,j,k} = x_{i,j,k} - \widetilde{x}_{i,j,k}, \tag{1}$$

and then mapped to a non-negative integer $\lambda_{i,j,k}$. The entropy encoder produces a code that represents $\lambda_{i,j,k}$ without loss. In the CCSDS-123 standard, one can choose between a sample- and a block-adaptive encoder.

B. ERROR CONTROL IN PREDICTIVE CODING SYSTEMS

For the encoder described above, the decoder can reproduce $x_{i,j,k}$, without loss. The addition of a quantizer provides higher compression ratios, but at the expense of some loss of fidelity in the decompressed image.

One of the simplest strategies to design a prediction-based compression algorithm that controls the maximum error produced is to quantize the prediction error $\Lambda_{i,j,k}$ with a quantizer Q, resulting in quantized version $\widehat{\Lambda}_{i,j,k}$ (and, in consequence, $\widehat{\lambda}_{i,j,k}$). The associated quantization index and its remapped version are denoted as $\Lambda^{Q}_{i,j,k}$ and $\lambda^{Q}_{i,j,k}$, respectively. Subsequent predictions $\widetilde{x}_{i,j,k}$ are calculated using previous reconstructed (lossy) samples $\widehat{x}_{i,j,k}$, which are obtained by implementing a decoder in the encoder [15], [22]. The decoder creates the reconstructed (lossy) image samples via:

$$\widehat{x}_{i,j,k} = \widehat{\Lambda}_{i,j,k} + \widetilde{x}_{i,j,k}. \tag{2}$$

Note that the errors in the reconstructed pixels are identical to the errors introduced by the quantizer in the prediction errors. That is, $x_{i,j,k} - \widehat{x}_{i,j,k} = \Lambda_{i,j,k} - \widehat{\Lambda}_{i,j,k}$. Thus, the errors in reconstructed pixels can be precisely controlled by controlling individual quantization errors. This is the basis of "near-lossless compression."

C. LIGHTWEIGHT BINARY ARITHMETIC CODER WITH CONTEXT MODEL

In a previous contribution [17] we introduced a compression system based on the CCSDS-123 predictor and a binary arithmetic encoder. The proposed entropy encoder works with binary symbols; let $b^{n}_{i,j,k}$ denote the n-th bit of the binary representation of $\lambda^{Q}_{i,j,k}$, with $N-1 \geq n \geq 0$. Here, N is chosen to provide a sufficient number of bits to represent all the $\lambda^{Q}_{i,j,k}$, with $b^{N-1}_{i,j,k}$ being the most significant bit. The entropy encoder makes use of context model patterns obtained using a context window that contains symbols coded previously to the current symbol. Further details can be found in [17].

D. RATE CONTROL

Bit allocation given a target bit-rate is a classical problem solved by rate control techniques [18]–[21], which distribute the bit budget for a collection of data elements in order to minimize the distortion D of the decoded image. If two elements are constrained to be encoded with R_{target} bits, the optimal allocation problem is typically formulated as:

$$\underset{Q_1,Q_2}{\operatorname{argmin}} \{D_1(Q_1) + D_2(Q_2)\} \tag{3}$$

$$\text{s.t. } R_1(Q_1) + R_2(Q_2) \leq R_{target}, \tag{4}$$

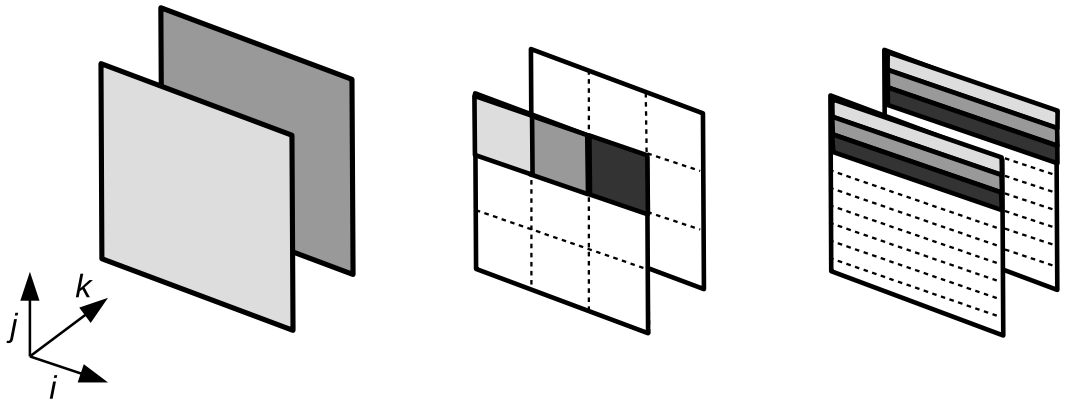

(a) band-by-band (b) block-by-block (c) spectral-line-by-spectral-line

FIGURE 2. Quantization structure comparison. Each gray intensity identifies a possibly different quantization step.

where D_i, Q_i and R_i represent the distortion, the quantization step size and the bit-rate corresponding to the i-th element, respectively. This formulation assumes independent quantization. That is, the distortion (rate) of the first element depends only on Q_1, and the distortion (rate) of the second element depends only on Q_2.

The problem of bit allocation given a target bit-rate for a dependent quantization coding system was proposed in [23] and was formulated as

$$\underset{Q_1,Q_2}{\text{argmin}} \{D_1(Q_1) + D_2(Q_1, Q_2)\} \tag{5}$$

$$\text{s.t. } R_1(Q_1) + R_2(Q_1, Q_2) \leq R_{target}. \tag{6}$$

Note that the distortion (rate) of the first element only depends on the quantization step employed for this element; while the distortion (rate) of the second element depends on the quantization step of the first and of the second element.

A solution to (6) can be obtained through Lagrange Multipliers by defining:

$$J_1(Q_1) = D_1(Q_1) + \lambda R_1(Q_1) \tag{7}$$

$$J_2(Q_1, Q_2) = D_2(Q_1, Q_2) + \lambda R_2(Q_1, Q_2) \tag{8}$$

and solving the following unconstrained minimization problem:

$$\underset{Q_1,Q_2}{\text{argmin}} \{J_1(Q_1) + J_2(Q_1, Q_2)\}, \tag{9}$$

and adjusting λ to satisfy (6). This can be extended to more than two dependent elements in the obvious way.

III. RATE-CONTROL HOMOGENIZING IMAGE QUALITY

Three rate control techniques have been recently designed for predictive image coding systems and assessed with CCSDS-123 coding. The first is [18], which divides the input image in blocks and applies different quantization steps to each block. The second is [19], in which quantization steps are determined band by band, instead of block by block. The third and most recent contribution is [20], which works in a spectral-line-by-spectral-line mode, assigning at each spectral line j a quantization step Q_j. Note that these works do not deal with ensuring constant error across all image regions since the quantization steps are set sequentially at the structure –block, band or spectral-line– level, employing a model function that relates the quantization steps with the rate, ignoring the image quality. Thus, adjacent structures are often reconstructed with different quality producing annoying quality irregularities. Section V provides examples of these irregularities. Figs. 2 (a), (b), and (c), depict the band-by-band, block-by-block, and spectral-line-by-spectral-line quantization, respectively.

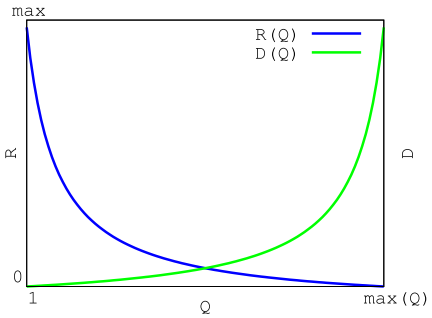

FIGURE 3. Monotonicity property of a Rate-Distortion function.

In order to 1) homogenize the quality of the decoded image, 2) maximize the image quality at a given target bit-rate, and 3) accurately yield effective bit rates close to R_{target}, a new rate control algorithm is proposed. The objective of the algorithm is to code the current line, generating quantized and entropy-coded versions of lines choosing those quantization steps that minimize error variations between lines and fit with the target bit-rate once all lines are processed.

For our proposed rate control algorithm, we smartly choose the quantization steps thanks to the monotonically increasing property between Q and D. This property relies on the fact that if the quantization step is increased, i.e., $Q_1 < Q_2$, then the distortion is also augmented, i.e., $D_1 < D_2$. On the other hand, the relation between Q and R is monotonically decreasing, for example, if the quantization step is increased, i.e., $Q_1 < Q_2$, then the rate is decreased, i.e., $R_1 > R_2$. Fig. 3

depicts the monotonic nature of a typical rate-distortion (RD) function.

This property allows to employ an iterative method to choose the appropriate quantization steps for each line, since we can set a quantization step for the first line $Q_{0,0}$ and adapt the step size for the rest of the lines $Q_{j,k}$ with $j > 0$ and $k > 0$ in order to homogenize the quality. If the produced codestream has a rate different than the target rate, $Q_{0,0}$ will be adapted, and the $Q_{j,k}$ for j and $k > 0$ will be modified producing a reconstructed quality as close as possible to $Q_{0,0}$. Thus, if the produced rate is higher or lower than the target rate, then $Q_{0,0}$ will be, respectively, increased or decreased.

To provide high image quality homogenization and rate accuracy, the proposed method deals with lines instead of bands, blocks, or spectral-lines. Lines are visited following the band interleaved by line order. That is, given a multi-band image, the first line of the first band is visited followed by the first line of the second band and so on. Scanning then proceeds to the second line of the first band.

A. RATE CONTROL ALGORITHM

Algorithm 1 describes the proposed rate-control strategy assuming the monotonically increasing property. It is based on three functional blocks: Predict($x_{j,k}$, $Q_{j,k}$), GetError($\widehat{\Lambda}_{j,k}$) and Encode($\widehat{\Lambda}_{j,k}$). The Predict($x_{j,k}$, $Q_{j,k}$) function is in charge of predicting the samples in line $x_{j,k}$ and quantizing the associated prediction error with a quantization step $Q_{j,k}$, and returning $\widehat{\Lambda}_{j,k}$. The GetError($\widehat{\Lambda}_{j,k}$) and Encode($\widehat{\Lambda}_{j,k}$) functions provide the error and the coding bit-rate and respectively return values $\text{MSE}_{j,k}$ and $R_{j,k}$. The error measure saved in $\text{MSE}_{j,k}$ is the Mean Square Error (MSE), calculated as

$$\text{MSE}_{j,k} = \frac{1}{I}\sum_{i=0}^{I-1}(x_{i,j,k} - \widehat{x}_{i,j,k})^2. \tag{10}$$

To recover an image with a very similar error among all the lines, the quantization steps must be selected carefully. This selection is introduced in the proposed algorithm through the following methodology:

1) The error of the first line ($k = 0$ and $j = 0$) obtained with a quantization step $Q_{0,0}$ is stored in $\text{MSE}_{0,0}$ (see lines 11-13).
2) For the remaining lines, $Q_{j,k}$ is adapted accordingly to obtain $\text{MSE}_{j,k}$ as close as possible to $\text{MSE}_{0,0}$. (see lines 16-29).
3) Once the quantization steps have been chosen for all the lines, the total achieved rate R is computed (line 33).
4) If R is close enough to the target rate – according to an error tolerance – the algorithm stops.
5) Otherwise, the algorithm continues in line 2. In this case, the quantization step size of the first line is increased or decreased according to the target rate and R, (see lines 4-7).

After the Algorithm is finished, the set of quantization step sizes $Q_{j,k}$ are employed to encode the image. Fig. 4 displays a band of a remote sensing image (left), the quantization steps sizes determined by our rate-control method (middle), and a more detailed discrimination of the step sizes (right). For the quantization steps plot, the vertical and horizontal axis represent the row and QSTEPS, respectively. As can be seen, our proposal applies larger step sizes to those regions containing regular textures (top areas) than those with greater intensity variations (bottom areas.)

It is worth noting that the proposed algorithm is devised to determine the best solution in terms of constant quality, not to minimize computational load. However, some aspects can be considered to speed up the execution. The contents of QSTEPS are selected in order to have a step size large enough to achieve the desired target rate. For high bit-rates, the values in QSTEPS can be reduced, containing only small step sizes.

Algorithm 1 Proposed Rate-Control Algorithm

Inputs: R_{target}, tolerance

1: $R = \infty$, $Q_0 = 0$
2: QSTEPS = {512, 256, 128, 64, 32, 16, 8, 4, 2, 1}
3: **for** *qstep* $= 0, \ldots,$ QSTEPS.*length* $- 1$ **do**
4: **if** $R < R_{\text{target}}$ **then**
5: $Q_0 \leftarrow Q_0 -$ QSTEPS[*qstep*]
6: **else**
7: $Q_0 \leftarrow Q_0 +$ QSTEPS[*qstep*]
8: **end if**
9: **for** $j = 0, \ldots, J-1$ **do**
10: **for** $k = 0, \ldots, K-1$ **do**
11: **if** $j = 0$ and $k = 0$ **then**
12: $\widehat{\Lambda}_{0,0} = \text{Predict}(x_{0,0}, Q_{0,0})$
13: $\text{MSE}_{0,0} = \text{GetError}(\widehat{\Lambda}_{0,0})$
14: $R_{0,0} = \text{Encode}(\widehat{\Lambda}_{0,0})$
15: **else**
16: **for** *qline* $= 0, \ldots,$ QSTEPS.*length* $- 1$ **do**
17: **if** *qline* $= 0$ **then**
18: $Q_{j,k} \leftarrow$ QSTEPS[*qline*]
19: **else**
20: **if** $\text{MSE}_{j,k} > \text{MSE}_{0,0}$ **then**
21: $Q_{j,k} \leftarrow Q_{j,k} -$ QSTEPS[*qline*]
22: **else**
23: $Q_{j,k} \leftarrow Q_{j,k} +$ QSTEPS[*qline*]
24: **end if**
25: **end if**
26: $\widehat{\Lambda}_{j,k} = \text{Predict}(x_{j,k}, Q_{j,k})$
27: $\text{MSE}_{j,k} = \text{GetError}(\widehat{\Lambda}_{j,k})$
28: $R_{j,k} = \text{Encode}(\widehat{\Lambda}_{j,k})$
29: **end for**
30: **end if**
31: **end for**
32: **end for**
33: $R \leftarrow \sum_{k=0}^{K-1}\sum_{j=0}^{J-1} R_{j,k}$
34: **if** $|R - R_{\text{target}}| <$ tolerance **then**
35: break execution
36: **end if**
37: **end for**

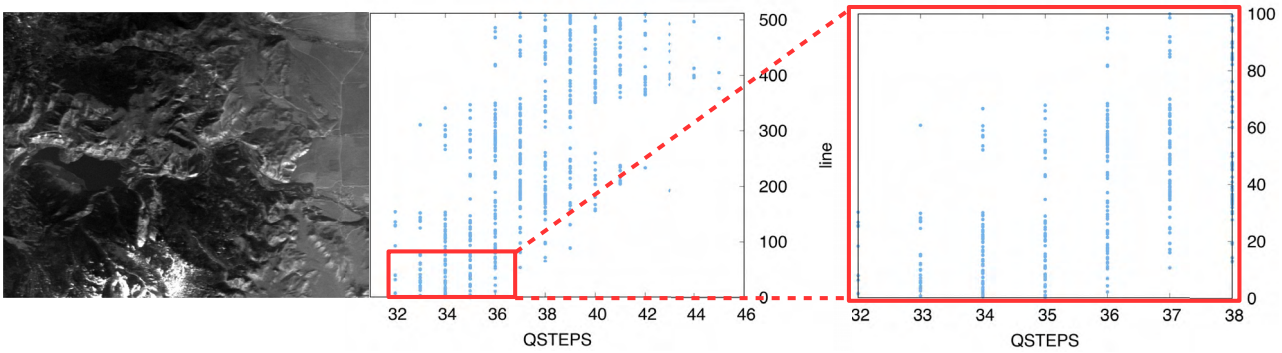

FIGURE 4. Graphical illustration of how quantization step sizes vary depending on the line to be encoded.

In addition, the higher the value of ''tolerance,'' the earlier the execution can be stopped (see line 34).

B. RATE ACCURACY

The rate control described in Algorithm 1 prioritizes uniform reconstruction quality over target rate accuracy. This effect is achieved by ensuring that all lines have similar quality before the global rate is evaluated. We refer to this rate control as *Mode 1*. Unfortunately, at high rates the achievable codestream lengths become sparser than at low rates, making it difficult to generate a final bitstream with an accurate rate with Mode 1. With the goal of obtaining higher rate accuracy, we introduce a variation in the algorithm referred to as *Mode 2*. Mode 2 works during the entropy encoder and after the Algorithm 1 is executed. In particular, Mode 2 measures how many bits have been used to encode previous lines and how many will be employed for the rest of the lines and adjusts the step sizes for the next lines to achieve the global target rate. This is detailed in Algorithm 2 below.

Algorithm 2 tracks the current real rate, referred as *RealRate*, to adapt $Q_{j,k}$ of the coming line according to the step_{inc} as follows: once the current line $x_{j,k}$ is predicted and entropy coded, the final rate R_{total} is estimated by the addition of *RealRate* –data already stored in the final bitstream– and $R_{j',k'}$, where j' and k' refer to the remaining lines not yet processed (see lines 6-11); then, depending on R_{total} and R_{target}, $Q_{j,k}$ is adapted according to step_{inc} (see lines 13-17). So as not to excessively increase the error difference between lines, step_{inc} is set to 1.

Although Mode 2 provides a finer rate accuracy, it can produce slight variations of the error between lines, not produced with Mode 1.

IV. ADOPTED CODING APPROACH

The novel rate control method may be incorporated in any coding system based on prediction; here, we incorporate it in the compressor pipeline of [17]. The new lossy and near-lossless coding system based on prediction is defined as follows. Once a line is scanned, predicted, and mapped to positive values, it is entropy encoded on a bitplane-by-bitplane basis employing a lightweight contextual arithmetic coder. The rate control presented here uses the quantized and dequantized predicted lines to know the current error of the

Algorithm 2 Proposed Rate-Control Algorithm With High Rate Accuracy

Inputs: R_{target}, step_{inc}, tolerance

1: $RealRate \leftarrow 0$
2: **for** $j = 0, \ldots, J-1$ **do**
3: **for** $k = 0, \ldots, K-1$ **do**
4: $R_{\text{total}} \leftarrow RealRate$
5: $k^* \leftarrow k$
6: **for** $j' = j, \ldots, J-1$ **do**
7: **for** $k' = k^*+, \ldots, K-1$ **do**
8: $R_{\text{total}} \leftarrow R_{\text{total}} + R_{j',k'}$
9: **end for**
10: $k^* \leftarrow 0$
11: **end for**
12: **if** $j = 0$ and $k = 0$ **then**
13: **if** $|R_{\text{total}} - R_{\text{target}}| >$ tolerance **then**
14: $Q_{j,k} \leftarrow Q_{j,k} - \text{step}_{\text{inc}}$
15: **else**
16: $Q_{j,k} \leftarrow Q_{j,k} + \text{step}_{\text{inc}}$
17: **end if**
18: **else**
19: **if** $|R_{\text{total}} - R_{\text{target}}| >$ tolerance **then**
20: **if** $R_{\text{total}} < R_{\text{target}}$ and $\text{MSE}_{0,0} < \text{MSE}_{j,k}$ **then**
21: $Q_{j,k} \leftarrow Q_{j,k} - \text{step}_{\text{inc}}$
22: **end if**
23: **if** $R_{\text{total}} > R_{\text{target}}$ and $\text{MSE}_{0,0} > \text{MSE}_{j,k}$ **then**
24: $Q_{j,k} \leftarrow Q_{j,k} + \text{step}_{\text{inc}}$
25: **end if**
26: **end if**
27: **end if**
28: $\widehat{\Lambda}_{j,k} = \text{Predict}(x_{j,k}, Q_{j,k})$
29: $RealRate \leftarrow RealRate + \text{Encode}(\widehat{\Lambda}_{j,k})$
30: $\text{MSE}_{j,k} = \text{GetError}(\widehat{\Lambda}_{j,k})$
31: **end for**
32: **end for**

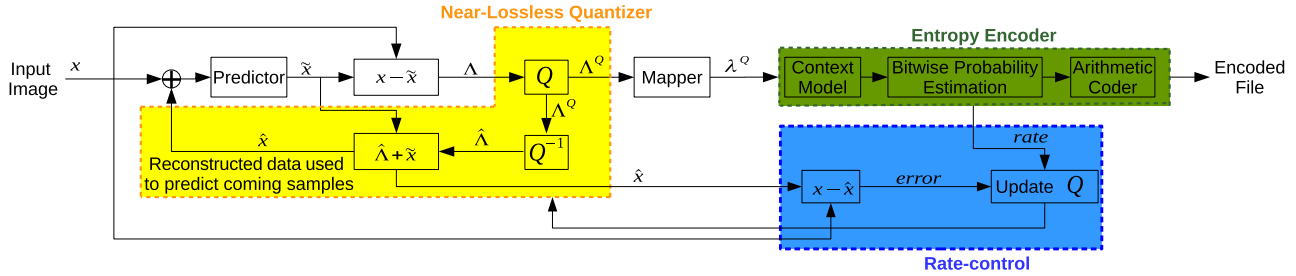

FIGURE 5. Proposed coding scheme.

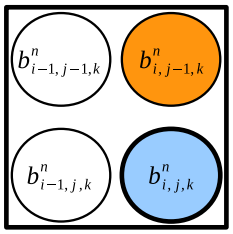

FIGURE 6. Illustration of context model used to encode $b^n_{i,j,k}$. $b^n_{i,j-1,k}$ is used as contextual data to estimate the probability.

line, and the entropy coder to figure out the number of bits needed for the current line. Thus, the rate control can adapt the step size to homogenize the image quality at a target bit-rate. It is worth noting that the proposed rate control can be employed with any predictor, quantizer or entropy encoder. Fig. 5 displays our proposed coding scheme.

The proposed coding scheme incorporates a Uniform Scalar Deadzone Quantizer (USDQ) that quantizes $\Lambda_{i,j,k}$ to obtain a quantized index according to

$$\Lambda^{Q}_{i,j,k} = \text{sign}(\Lambda_{i,j,k}) \left\lfloor \frac{|\Lambda_{i,j,k}|}{Q_{j,k}} \right\rfloor, \tag{11}$$

where the quantization step is Q. The operation to reconstruct $\hat{\Lambda}_{i,j,k}$ from its quantization index is expressed as

$$\hat{\Lambda}_{i,j,k} = \text{sign}(\Lambda^{Q}_{i,j,k})(Q_{j,k} + \delta)\Lambda^{Q}_{i,j,k}, \tag{12}$$

with δ equal to 0.5 for $Q_{j,k} > 1$. USDQ has been selected due to its straightforward implementation and excellent performance, e.g., in the JPEG 2000 standard [24]. USDQ partitions the range of input values into intervals all of size $Q_{j,k}$, except for the interval that contains zero, which is of size $2Q_{j,k}$. This results in all absolute pixel errors $| x_{i,j,k} - \widehat{x}_{i,j,k} |$ being bounded above by $Q_{j,k}$.

Like the entropy encoder presented in [17], we make use of a context model to estimate the conditional probability with which the current bit $b^n_{i,j,k}$ is encoded. According to [17], we only consider the sample above the bit to be encoded as contextual information. This is indicated in Fig. 6. The initial probability model for the context is set to a value of 0.66.

Further details of the context model and conditional probability estimation are described in [17].

V. EXPERIMENTAL RESULTS

For the experiments conducted in this work, we have selected a set of varied data formed by remote sensing, medical and natural images. Their names and main features are listed in Table 1. The first order entropy represents the entropy of individual pixels, without accounting for any dependencies among pixels within or between bands.

In [25], the impact of different CCSDS-123 parameters that control the operation of the prediction and the entropy encoder were evaluated, suggesting that a correct parameter selection has more impact on the predictor stage than in the entropy encoder stage. Concerning the prediction, local sum type, prediction mode, number of prediction bands, and predictor adaption were the most critical parameters. Extensive experimental evaluations were conducted to find suitable configurations. In the current manuscript, leaning on results of [25] and after conducting also an extensive evaluation, experimental results are produced for the following parameter configuration: predictor mode and local sum type depend on the acquisition sensor for the remote sensing images, whereas for medical and natural data the same configuration is utilized. When $K > 1$, the number of prediction bands P is set to 3, the predictor adaptation rate ν_{max} is set to 3, since, in general, it yields the best performance.

For the proposed rate control technique, the tolerance variable of Mode 1 and the step_{inc} of Mode 2 are fixed to 0.01 and 1, respectively.

In order to yield a fair comparison between the proposed rate-control technique and the latest rate-control contribution designed for encoding systems based on prediction [20], we substituted the rate-control technique (blue box) of the proposed coding scheme, depicted in Fig. 5, by the rate-control technique proposed in [20]. In this way, assessment of both rate-control techniques is equitable since both employ the same predictor, quantizer and entropy encoder. We named this new method [20]′.

To compare the proposed prediction-based coding system with transform-based coding systems, we also provide results for JPEG2000 [26] and CCSDS-122 [27]. We have employed the Reversible Karhunen-Loeve transform (RKLT) to decorrelate the spectral dimension yielding as fair a comparison as possible among the four evaluated coding techniques.

The rest of this section appraises the performance of our proposal in terms of 1) rate accuracy, 2) minimization of the

TABLE 1. Data used in the experimental results. Image name, its abbreviation, bit-depth and first-order entropies (in bps). The last two columns indicate the predictor mode and the local sum used in the proposed coding system for each sensor.

Image Name	Abbreviation	Dimensions	bit-depth	Entropy	Predictor Mode	Local Sum
Remote Sensing Images						
aviris_yellowstone_f060925t01p00r12_sc00_uncal	yellowstoneU	224x512x680	13	11.06	Neighbor Oriented	Full Mode
Hyperion_Cuprite_level0	cuprite	242x1024x256	12	6.87	Column Oriented	Reduced Mode
M3_globalA	globalA	86x512x320	12	7.60	Column Oriented	Reduced Mode
Landsat_agriculture	agriculture	6x1024x1024	8	8.00	Neighbor Oriented	Full Mode
Medical Images						
angio_03508649	angio_1	64x512x512	12	10.52	Neighbor Oriented	Full Mode
CT0030	CT30	240x512x512	12	8.78	Neighbor Oriented	Full Mode
hemo_47042664	hemo_1	14x1024x1024	12	9.67	Neighbor Oriented	Full Mode
Natural Images						
ISO_12640-1-portrait	portrait	1x2560x2048	8	7.42	Neighbor Oriented	Full Mode
ISO_12640-1-Cafeteria	cafeteria	1x2560x2048	8	7.74	Neighbor Oriented	Full Mode
guitar	guitar	3x2448x2448	16	15.15	Neighbor Oriented	Full Mode

TABLE 2. Output Rates comparison between Mode 1 and Mode 2. For the *guitar* image the target rates are doubled. (*): Lossless.

		Target rates			
Image	Rate Control	1 bps	2 bps	3 bps	4 bps
yellowstoneU	Mode 1	1.06	1.99	3.00	4.11
	Mode 2	1.04	2.00	3.00	4.01
cuprite	Mode 1	1.02	1.89	3.14	4.34*
	Mode 2	1.01	2.00	3.01	4.01
globalA	Mode 1	0.90	2.21*	2.21*	2.21*
	Mode 2	0.99	2.01	2.21*	2.21*
agriculture	Mode 1	1.04	1.83	2.45	3.64*
	Mode 2	1.01	2.00	3.00	3.64*
angio_1	Mode 1	1.02	2.01	3.05	4.18
	Mode 2	1.01	2.01	3.01	4.01
CT30	Mode 1	0.94	2.05	3.10	3.89
	Mode 2	0.97	2.01	3.01	4.00
hemo_1	Mode 1	1.05	2.01	3.01	4.18
	Mode 2	1.01	2.01	3.01	4.01
portrait	Mode 1	0.99	1.99	2.77	4.58*
	Mode 2	1.00	2.00	3.00	4.01
cafeteria	Mode 1	1.01	2.01	2.92	4.37
	Mode 2	1.01	2.01	3.00	4.01
guitar	Mode 1	2.05	4.02	6.06	7.82
	Mode 2	2.04	4.01	6.01	8.00

error gap between lines, 3) rate-distortion performance; and 4) visual inspection.

A. RATE ACCURACY EVALUATION

These results serve to evaluate the accuracy of the rate control in terms of output rate. This test is conducted for a set of images from distinct scenarios and four different target bit-rates with Mode 1 and Mode 2. Table 2 reports the output rates achieved for four target bit-rates. Though Mode 1 is less accurate than Mode 2, it can still obtain output rates with suitable precision for most of the target rates. Mode 2 always has remarkably good accuracy due to the information collected by the rate control algorithm in $R_{j,k}$, which permits to adapt the current quantization step and better estimate future output rates. In Mode 2, larger step_{inc} values can produce output rates with higher accuracy, at the expense of generating major error differences between adjacent lines. It can be seen that the algorithm performs equally well independently of the image corpus, either remote sensing, medical or natural images. And, in addition, Mode 1 and Mode 2 produce a maximum error in the output rates of 14% –portrait at 4 bps– and 3% –CT30 at 1 bps–, respectively.

B. CONSTANT QUALITY EVALUATION

These experiments demonstrate that the bit budget allocated by our proposal produces homogeneous quality recovery.

The first experiment reported is displayed in Fig. 7. This figure plots the MSE for each line and band employing a color scale. The horizontal and vertical axis denote bands and lines, respectively. The MSE is represented by a color scale, with yellow and black for, respectively, the highest and the lowest MSE values. Fig. 7 provides results at four different target bit-rates (one per column). The first three rows of the figure correspond to a remote sensing image, whereas the last three correspond to a medical image. For each bit-rate, results are reported for [20]′, and our proposal employing either Mode 1 or Mode 2. Note that the color scale is different for each image and bit-rate but the same between schemes. From these results, we can appreciate that:

1) Mode 1 obtains the image quality with the highest homogeneity.
2) Mode 1 and Mode 2 attain much lower MSE variation than [20]′. The large differences in [20]′ are produced because in the rate control defined in [20], the first row ($j = 0$) is encoded without loss, then the quantization steps are adapted to reach the desired target bit rate.
3) Mode 2 has a higher MSE fluctuation compared with Mode 1. This is produced since Mode 2 sets the step_{inc} to 1, adapting the quantization step with $+/-$ 1 to achieve the target bit-rate with higher accuracy. Nevertheless, the error variation is still much lower than for [20]′.

Equivalent results are obtained for the other types of images tested in our experiments.

The second experiment provides the Mean Unsigned Deviation (MUD) of the MSE metric. MUD provides the average

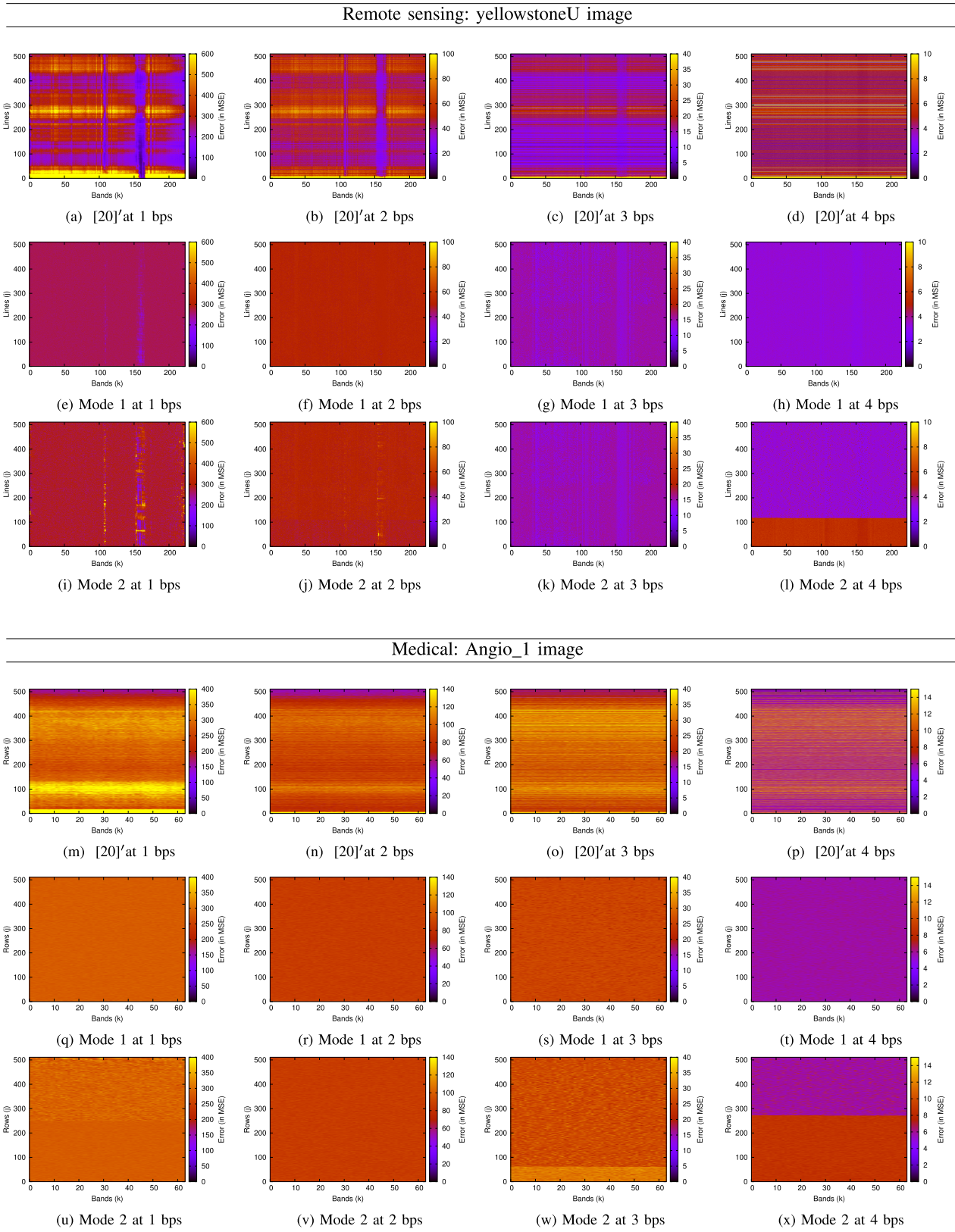

FIGURE 7. Error (in MSE) plotted for each row *j* and band *k* at target rates of 1, 2, 3, and 4 bps. Results are showed for [20]′, Mode 1 and Mode 2. Plots from (a) to (l) and from (m) to (x) belong to yellowstoneU and Angio_1, respectively.

TABLE 3. MUD comparison of the row-by-row MSE between Mode 1, Mode 2, and [20]′. For the *bananas* image the target rates are doubled. (*): Lossless.

Image	Rate Control	1 bps	2 bps	3 bps	4 bps
yellowstoneU	Mode 1	6.77	1.99	1.31	0.11
	Mode 2	35.78	6.70	3.88	1.57
	[20]′	526.68	49.78	6.34	2.25
cuprite	Mode 1	0.82	0.28	0.02	0.00*
	Mode 2	2.44	1.75	0.48	0.21
	[20]′	4.62	2.00	1.07	0.54
globalA	Mode 1	0.08	0.00*	0.00*	0.00*
	Mode 2	1.00	0.21	0.00*	0.00 *
	[20]′	13.81	4.08	0.00 *	0.00*
agriculture	Mode 1	0.34	0.05	0.01	0.00*
	Mode 2	1.57	1.17	0.73	0.00*
	[20]′	2.41	4.24	0.93	0.00*
angio_1	Mode 1	4.77	2.59	1.17	0.31
	Mode 2	16.76	9.07	4.80	2.99
	[20]′	633.32	13.12	6.09	3.17
CT30	Mode 1	4.35	1.05	0.23	0.06
	Mode 2	8.26	3.83	1.84	1.39
	[20]′	64.40	12.00	4.15	1.41
hemo_1	Mode 1	1.97	1.49	0.25	0.04
	Mode 2	7.35	5.05	2.93	0.91
	[20]′	43.53	15.02	5.14	2.60
portrait	Mode 1	0.80	0.19	0.03	0.00*
	Mode 2	3.52	1.76	1.24	0.25
	[20]′	29.78	6.13	4.09	1.69
cafeteria	Mode 1	60.86	9.77	2.58	0.25
	Mode 2	60.86	9.77	2.35	0.56
	[20]′	75.08	14.43	4.07	1.83
guitar	Mode 1	65.26	7.57	0.62	0.04
	Mode 2	210.47	17.49	4.14	1.46
	[20]′	6969.69	433.87	25.69	2.32

of the absolute MSE deviations from the mean MSE. It is computed in a row-by-row way as

$$\mathrm{MUD} = \frac{1}{J \times K} \sum_{j=0}^{J-1} \sum_{k=0}^{K-1} |\overline{\mathrm{MSE}} - \mathrm{MSE}_{j,k}|, \qquad (13)$$

where $\mathrm{MSE}_{j,k}$ is computed as (10) and $\overline{\mathrm{MSE}}$ is computed as

$$\overline{\mathrm{MSE}} = \frac{1}{J \times K} \sum_{j=0}^{J-1} \sum_{k=0}^{K-1} \mathrm{MSE}_{j,k}. \qquad (14)$$

For the MUD metric, lower is better.

Table 3 reports the MUD metric for images from different scenarios at different rates. It can be observed that:

1) Mode 1 obtains the lowest MUD value, followed by Mode 2.
2) At lower bit-rates, the differences between the three techniques are larger than at higher bit-rates. This trend is emphasized for images with higher entropy such as *yellowstoneU*, *angio_1*, and *guitar*.
3) Although at higher rates the MUD differences between our proposal and [20]′ are reduced substantially, our proposal gets the best results in all cases.

C. RATE-DISTORTION EVALUATION

The tests reported in this section are aimed to evaluate the rate-distortion performance of Mode 1 and Mode 2 of our proposal with respect to the near-lossless coding technique introduced in [17]. Fig. 8 shows the rate SNR and rate MUD curves for a remote sensing and a medical image compressed with Mode 1, Mode 2 and [17]. As [17] is a near-lossless compressor, images are encoded and decoded at different quantization steps, then the rate and the SNR and MUD are computed and used to interpolate the curves. All results are produced using the same predictor and entropy encoder configuration. The following definition of SNR (SNR Energy) is employed in this work:

$$\mathrm{SNR} = 10 \log_{10} \frac{\sum_{i=0}^{I-1} \sum_{j=0}^{J-1} \sum_{k=0}^{K-1} {x_{i,j,k}}^2}{\sum_{i=0}^{I-1} \sum_{j=0}^{J-1} \sum_{k=0}^{K-1} (x_{i,j,k} - \widehat{x}_{i,j,k})^2}, \qquad (15)$$

measured in *dB*, where x and $\widehat{x}$ denote the original and reconstructed samples, respectively.

From Fig. 8 we can see that: 1) Modes 1 and 2 provide nearly the same rate-distortion performance as the near-lossless technique (Fig. 8 (a) and (c)). 2) For MUD plots (Fig. 8 (b) and (d)) Mode 1 obtains the best performance. 3) Again for MUD plots, for bit-rates larger than 1.5 and 0.5 bps for *globalA* and *angio_1* images, respectively, all evaluated techniques produce almost the same performance. And, 4) the curves of Mode 1 and [17] for *globalA* at rates larger than 1.2 bps provide lossless recovery. This is produced because in [17] there is no control of the final rate, whereas for Mode 1 the selection of the quantization steps prioritizes the image quality instead of building code-streams with high-rate accuracy, and with a target rate of 2 bps, lossless compression is obtained.

The last experiment in this section compares the performance of Mode 2 and [20]′ against wavelet transform coding techniques in terms of rate accuracy, Peak Absolute Error (PAE) and SNR quality metrics. Table 4 reports a comparison between Mode 2, [20]′, RKLT+JPEG2000 and RKLT+CCSDS-122. The best results for PAE and SNR between the rate control proposed here and [20]′ are highlighted in bold font. This evaluates the same predictive coding employing different rate control techniques. The best results between our proposal, RKLT+JPEG2000 and RKLT+CCSDS-122 are underlined. These results suggest that:

1) Mode 2 yields the lowest PAE in all cases. For the *guitar* image, our proposal reaches gains superior to 300, 220, and 145 units compared with, respectively, [20]′, RKLT+JPEG2000, and RKLT+CCSDS-122.
2) Our proposal gets higher SNR than [20]′ for all rates and images, achieving gains of more than 12 dB for *globalA* at 2 bps.
3) Coding techniques based on transform produce better SNR for most rates and images, but with significantly larger PAE values than the proposed Mode 2.

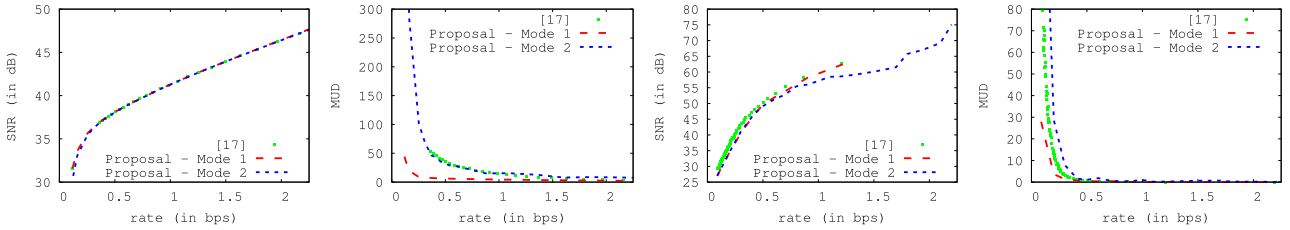

FIGURE 8. Rate SNR and Rate MUD-MSE curves for angio_1 ((a) and (b)), and globalA ((c) and (d)).

TABLE 4. Output rates, PAE and SNR image quality comparison. Results are provided for Mode 2 of our proposal, [20]′, RKLT+JPEG2000, and RKLT+CCSDS-1222. Target rates evaluated are 1, 2, 3 and 4 bps, except for *guitar*, where rates are doubled.

		Proposed with Mode 2			[20]′			RKLT+JPEG2000			RKLT+CCSDS-122		
Image	Target (bps)	Rate	PAE	SNR	Rate	PAE	SNR	Rate	PAE	SNR	Rate	PAE	SNR
yellowstoneU	1	1.000	**131**	**48.67**	1.000	512	45.73	1.020	140	55.06	1.067	187	54.02
	2	2.000	**43**	**56.07**	2.000	162	54.48	2.014	45	59.23	2.070	49	58.04
	3	3.000	**9**	**61.56**	3.000	34	60.99	2.974	20	63.48	3.073	25	62.48
	4	4.000	**4**	**67.23**	4.000	12	66.31	4.021	12	67.68	4.075	14	66.88
cuprite	1	1.000	**21**	**45.00**	1.000	78	44.71	1.029	39	46.30	1.075	63	44.43
	2	2.000	**7**	**50.90**	2.000	32	50.75	2.029	14	49.52	2.080	19	48.39
	3	3.000	**2**	**55.40**	3.000	16	54.37	2.980	14	51.57	3.082	14	50.96
	4	4.000	**1**	**64.71**	4.000	6	61.13	4.029	13	53.33	4.085	13	53.01
globalA	1	1.000	**4**	**57.15**	0.998	415	49.78	1.012	59	53.20	1.064	139	40.70
	2	2.000	**1**	**67.83**	2.000	80	55.73	2.005	13	57.25	2.069	38	52.32
	3	2.213	**0**	**Infinity**	2.213	**0**	**Infinity**	2.980	7	58.34	3.072	10	56.08
	4	2.213	**0**	**Infinity**	2.213	**0**	**Infinity**	3.653	0	Infinity	4.073	8	58.09
agriculture	1	1.000	**7**	**29.01**	1.000	28	28.91	0.987	15	32.49	1.047	19	31.69
	2	2.000	**3**	**35.92**	2.000	34	31.84	2.001	7	35.78	2.050	8	35.30
	3	3.000	**2**	**40.37**	3.000	8	38.59	3.001	5	38.48	3.053	6	37.94
	4	3.638	**0**	**Infinity**	3.638	**0**	**Infinity**	3.670	0	Infinity	3.919	0	Infinity
angio_1	1	1.000	**45**	**41.13**	1.000	512	37.86	0.991	39	46.30	1.075	63	44.43
	2	2.000	**21**	**46.37**	2.000	46	46.26	1.989	14	49.52	2.080	19	48.39
	3	3.000	**10**	**51.34**	3.000	22	51.26	2.959	14	51.57	3.082	14	50.96
	4	4.000	**6**	**56.71**	4.000	10	56.65	3.956	13	53.33	4.085	13	53.01
CT30	1	0.970	**93**	**36.43**	1.000	158	35.92	1.074	165	39.53	1.074	260	39.21
	2	2.000	**12**	**43.47**	2.000	20	42.95	2.078	41	45.67	2.078	59	45.72
	3	3.000	**6**	**49.34**	2.999	10	48.66	3.085	21	49.60	3.085	20	49.89
	4	4.000	**3**	**54.66**	4.000	6	54.40	4.089	15	51.99	4.089	14	52.39
hemo_1	1	1.000	**25**	**45.97**	1.000	139	45.49	0.999	57	47.74	1.047	80	46.63
	2	2.000	**12**	**51.07**	2.000	62	50.44	2.000	28	52.42	2.050	38	51.17
	3	3.000	**7**	**55.95**	3.000	30	55.36	2.972	19	56.99	3.053	24	55.95
	4	4.000	**3**	**61.19**	4.000	14	60.23	3.969	10	61.15	4.055	11	60.47
portrait	1	1.000	**21**	**27.33**	1.000	36	26.01	1.000	26	32.00	1.045	40	30.81
	2	2.000	**6**	**34.60**	2.000	18	32.81	2.000	11	37.49	2.049	12	36.30
	3	3.000	**3**	**39.76**	3.000	42	35.61	2.997	6	41.76	3.055	7	40.23
	4	4.000	**1**	**47.95**	4.000	36	40.57	3.999	2	46.78	4.056	5	45.04
cafeteria	1	1.000	**32**	**20.68**	1.006	108	20.12	0.999	90	25.48	1.045	81	24.17
	2	2.000	**10**	**28.62**	2.010	48	27.38	1.999	20	32.27	2.049	21	31.42
	3	3.000	**5**	**34.81**	3.002	26	33.04	3.000	10	37.30	3.054	11	36.09
	4	4.000	**2**	**41.19**	4.012	20	36.65	3.999	5	41.58	4.058	7	40.23
guitar	2	2.016	**208**	**48.41**	2.000	512	47.17	1.999	435	53.04	2.048	353	54.20
	4	4.000	**44**	**61.03**	4.000	512	59.50	3.999	84	65.24	4.059	86	65.86
	6	6.000	**11**	**73.06**	6.000	68	71.71	5.991	22	76.53	6.060	28	77.45
	8	8.000	**3**	**85.38**	8.000	16	83.38	7.993	6	86.44	8.060	8	87.34

D. VISUAL INSPECTION

The last experiment provides a visual comparison from an image encoded at 0.25 bps with Mode 2 and [20]′. Although Mode 1 provides better homogenized global error, we have employed Mode 2 in this experiment to attain the best target bit-rate accuracy. The original image is portrayed as a reference. Fig. 9, Fig. 10, and Fig. 11 show a band for a remote sensing, a medical, and a natural image, respectively.

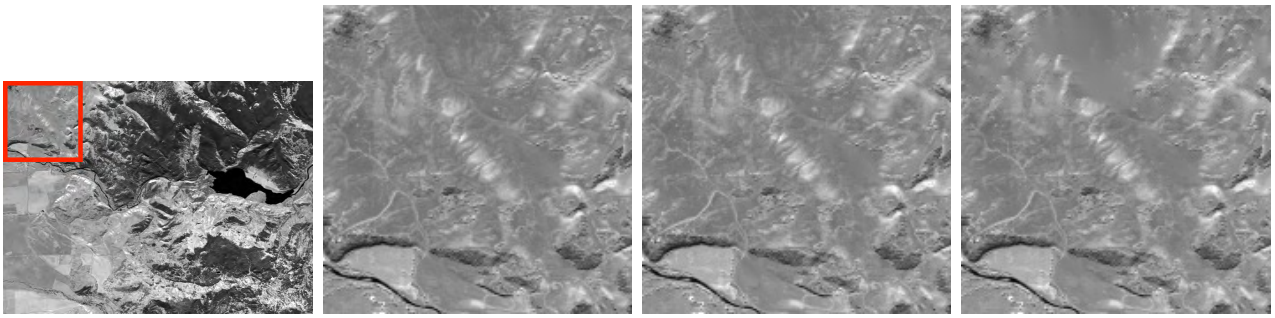

(a) (b) (c) (d)

FIGURE 9. Visual comparison for the yellowstoneU image. (a) Original, (b) original (crop), (b) proposed approach - Mode 2 at 0.25 bps (SNR = 30.06 dB.), and (d) [20]′at 0.25 bps (SNR = 28.54 dB.).

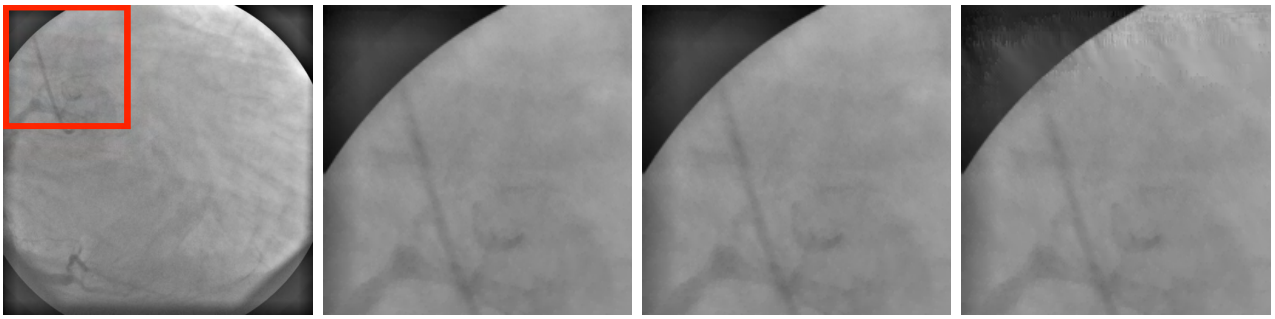

(a) (b) (c) (d)

FIGURE 10. Visual comparison for the angio_2 image. (a) Original, (b) original (crop), (c) proposed approach - Mode 2 at 0.25 bps (SNR = 36.56 dB.), and (d) [20]′ at 0.25 bps (SNR = 32.79 dB.).

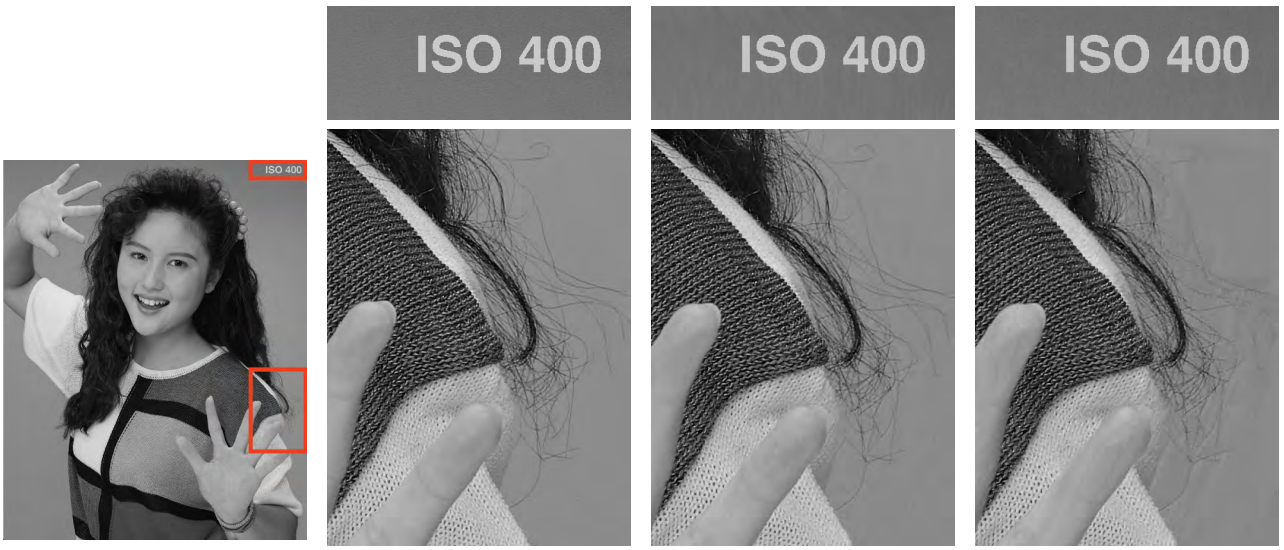

(a) (b) (c) (d)

FIGURE 11. Visual comparison for the portrait image. (a) Original, (b) original (crop), (c) proposed approach - Mode 2 at 1.5 bps (SNR = 31.60 dB.), and (d) [20]′ at 1.5 bps (SNR = 29.81 dB.).

The reader is invited to zoom in to see the specific visual artifacts arising from the different compression methods.

Although for the remote sensing and medical images we have encoded the images at low bit-rates, the difference of Fig. 9 and Fig. 10 between the original and the images encoded with our proposal are hard to appreciate visually. On the other hand, we can appreciate visual variations between our proposal and [20]′. These differences are more relevant in the firsts lines –top of the image–, which is motivated because of the adaptation of the quantization steps.

For the natural image, reconstructions at 1.5 bps are portrayed. Two different crop regions are showed. For the top-crop we can appreciate that [20]′ produces a degradation of the image quality, this behavior in the first lines forces [20]′ to more aggressively quantize the coming lines –bottom-crop– to achieve the target bit-rate. As seen, our proposal recovers the full image with homogeneous quality, higher fidelity and lower artifacts than [20]′.

VI. CONCLUSIONS

Though rate control techniques are easy to be enforced in transform coding techniques, this is not true in predictive image coding systems because of the intricate mathematical relation between the rate and the quantized residuals. There exist few contributions aimed at controlling the rate for image predictive coding systems; they estimate the rate given a quantization step through a modeling function, however they can not secure constant quality along the image. This manuscript introduces an iterative rate control algorithm for image coding systems based on prediction with the main goal of yielding constant quality for the entire reconstructed image. To provide constant quality, we propose an iterative rate control strategy that sets a quantization for the first line and adapts the further steps to yield uniform quality. In the case that the target bit-rate is not achieved, the step size of the first line is updated and the procedure is repeated. Our method obtains superior performance in terms of constant quality Peak Absolute Error (PAE) compared with the latest rate control technique for predictive image coding systems [20] and compared with transform coding methods such as JPEG2000 and CCSDS-122 (both preceded by the Reversible Karhunen-Loeve transform). Furthermore, our contribution provides higher Signal Noise Ratio (SNR) than [20] and, in some cases, it also outperforms JPEG2000 and CCSDS-122.

REFERENCES

[1] *JPEG-LS Lossless and Near-Lossless Compression for Continuous-Tone Still Images*, Standard ISO/IEC 14495-2:2003, 1999.

[2] *Joint Photographic Experts Group (JPEG)*. Accessed: Jul. 2019. [Online]. Available: http://www.jpeg.org

[3] Digital Image and Communication in Medicine. (Jan. 2019). *DICOM*. [Online]. Available: http://medical.nema.org/

[4] *Lossless Multispectral & Hyperspectral Image Compression*, document CCSDS-123.0-B-1 Blue Book, May 2012.

[5] *Consultative Committee for Space Data Systems (CCSDS)*. Accessed: Jul. 2019. [Online]. Available: http://www.ccsds.org

[6] F. Rizzo, B. Carpentieri, G. Motta, and J. A. Storer, "Low-complexity lossless compression of hyperspectral imagery via linear prediction," *IEEE Signal Process. Lett.*, vol. 12, no. 2, pp. 138–141, Feb. 2005.

[7] J. Song, Z. Zhang, and X. Chen, "Lossless compression of hyperspectral imagery via RLS filter," *Electron. Lett.*, vol. 49, no. 16, pp. 992–994, Aug. 2013.

[8] W. Jiaji, K. Wanqiu, M. Jarno, and H. Bormin, "Lossless compression of hyperspectral imagery via clustered differential pulse code modulation with removal of local spectral outliers," *IEEE Signal Process. Lett.*, vol. 22, no. 12, pp. 2194–2198, Dec. 2015.

[9] F. Gao and S. Guo, "Lossless compression of hyperspectral images using conventional recursive least-squares predictor with adaptive prediction bands," *J. Appl. Remote Sens.*, vol. 10, no. 1, 2016, Art. no. 015010.

[10] N. Amrani, J. Serra-Sagristà, V. Laparra, M. W. Marcellin, and J. Malo, "Regression wavelet analysis for lossless coding of remote-sensing data," *IEEE Trans. Geosci. Remote Sens.*, vol. 54, no. 9, pp. 5616–5627, Sep. 2016.

[11] E. Magli, G. Olmo, and E. Quacchio, "Optimized onboard lossless and near-lossless compression of hyperspectral data using CALIC," *IEEE Geosci. Remote Sens. Lett.*, vol. 1, no. 1, pp. 21–25, Jan. 2004.

[12] G. Carvajal, B. Penna, and E. Magli, "Unified lossy and near-lossless hyperspectral image compression based on JPEG 2000," *IEEE Geosci. Remote Sens. Lett.*, vol. 5, no. 4, pp. 593–597, Oct. 2008.

[13] C.-W. Chen, T.-C. Lin, S.-H. Chen, and T.-K. Truong, "A near lossless wavelet-based compression scheme for satellite images," in *Proc. WRI World Congr. Comput. Sci. Inf. Eng.*, vol. 6. Mar. 2009, pp. 528–532.

[14] S.-C. Tai, T.-M. Kuo, C.-H. Ho, and T.-W. Liao, "A near-lossless compression method based on CCSDS for satellite images," in *Proc. Int. Symp. Comput., Consum. Control*, 2012, pp. 706–709.

[15] I. Blanes, E. Magli, and J. Serra-Sagrista, "A tutorial on image compression for optical space imaging systems," *IEEE Geosci. Remote Sens. Mag.*, vol. 2, no. 3, pp. 8–26, Sep. 2014.

[16] J. Beerten, I. Blanes, and J. Serra-Sagristà, "A fully embedded two-stage coder for hyperspectral near-lossless compression," *IEEE Geosci. Remote Sens. Lett.*, vol. 12, no. 8, pp. 1775–1779, Aug. 2015.

[17] J. Bartrina-Rapesta, I. Blanes, F. Aulí-Llinàs, J. Serra-Sagristà, V. Sanchez, and M. W. Marcellin, "A lightweight contextual arithmetic coder for on-board remote sensing data compression," *IEEE Trans. Geosci. Remote Sens.*, vol. 55, no. 8, pp. 4825–4835, May 2017.

[18] D. Valsesia and E. Magli, "A novel rate control algorithm for onboard predictive coding of multispectral and hyperspectral images," *IEEE Trans. Geosci. Remote Sens.*, vol. 52, no. 10, pp. 6341–6355, Oct. 2014.

[19] M. Conoscenti, R. Coppola, and E. Magli, "Constant SNR, rate control, and entropy coding for predictive lossy hyperspectral image compression," *IEEE Trans. Geosci. Remote Sens.*, vol. 54, no. 12, pp. 7431–7441, Dec. 2016.

[20] D. Valsesia and E. Magli, "Fast and lightweight rate control for onboard predictive coding of hyperspectral images," *IEEE Geosci. Remote Sens. Lett.*, vol. 14, no. 3, pp. 394–398, Mar. 2017.

[21] Y. Shoham and A. Gersho, "Efficient bit allocation for an arbitrary set of quantizers [speech coding]," *IEEE Trans. Acoust., Speech, Signal Process.*, vol. 36, no. 9, pp. 1445–1453, Sep. 1988.

[22] N. S. Jayant and P. Noll, *Digital Coding of Waveforms*. Upper Saddle River, NJ, USA: Prentice-Hall, 1984.

[23] K. Ramchandran, A. Ortega, and M. Vetterli, "Bit allocation for dependent quantization with applications to multiresolution and MPEG video coders," *IEEE Trans. Image Process.*, vol. 3, no. 5, pp. 533–545, Sep. 1994.

[24] *Information Technology—JPEG 2000 Image Coding System—Part 1: Core Coding System*, Standard ISO/IEC 15444-1:2000, Dec. 2000.

[25] E. Augé, J. E. Sánchez, A. B. Kiely, I. Blanes, and J. Serra-Sagrista, "Performance impact of parameter tuning on the CCSDS-123 lossless multi- and hyperspectral image compression standard," *J. Appl. Remote Sens.*, vol. 7, no. 1, 2013, Art. no. 074594.

[26] D. S. Taubman and M. Marcellin, *JPEG2000: Image Compression Fundamentals, Standards and Practice*. Norwell, MA, USA: Kluwer, 2002.

[27] *Image Data Compression*, document CCSDS-122.0-B-1, Blue Book, Nov. 2005.

JOAN BARTRINA-RAPESTA received the B.Sc., B.E., M.S., and Ph.D. degrees in computer science from the Universitat Autònoma de Barcelona (UAB), Spain, in 2002, 2004, 2006, and 2009, respectively. He received the M.S. and Ph.D. degrees (Hons.) from UAB. He has received a Doctoral Fellowship from UAB. He has coauthored numerous papers in journals and conferences. He has guided Ph.D. students. Since 2012, he has been an Associate Professor with the Department of Information and Communications Engineering, UAB. His research interest includes a wide range of image coding topics, computing, and transmission. He participates as a Reviewer for magazines and symposiums.

MICHAEL W. MARCELLIN (S'81–M'87–SM'93–F'02) received the B.S. degree in electrical engineering from San Diego State University, in 1983, and the M.S. and Ph.D. degrees in electrical engineering from Texas A&M University, in 1985 and 1987, respectively. Since 1988, he has been with the University of Arizona, where he currently holds the title of Regents' Professor. He is also the International Foundation for Telemetering Chaired Professor. His research interests include digital communication and data storage systems, data compression, and signal processing. He has authored or coauthored over 300 publications in his research areas. He has received numerous honors including ten teaching awards.

JOAN SERRA-SAGRISTÁ (S'97–M'05–SM'11) received the Ph.D. degree in computer science from the Universitat Autònoma de Barcelona (UAB), Spain, in 1999. He is currently an Associate Professor (Habilitation Full professor) with the Department of Information and Communications Engineering, UAB. From 1997 to 1998, he was with the University of Bonn, Germany, supported by the DAAD. His current research interests include data compression, with special attention to image coding for remote sensing applications. He has coauthored over 100 publications. He was a recipient of the Spanish Intensification Young Investigator Award, in 2006. He serves or has served as Associate Editor for the IEEE TRANSACTIONS ON GEOSCIENCE AND REMOTE SENSING and the IEEE TRANSACTIONS ON IMAGE PROCESSING. He has served as the Committee Chair for Data Compression Conference.

MIGUEL HERNÀNDEZ-CABRONERO received the B.Sc. degree in computer science in mathematics from the Universitat Autónoma de Madrid, in 2010, and the M.Sc. and Ph.D. degrees *(cum laude)* in computer science from the Universitat Autònoma de Barcelona (UAB), in 2011 and 2015, respectively. He has carried Postdoctoral research stages with the University of Warwick, U.K., and the University of Arizona, USA. He is currently with the Department of Information and Communications Engineering, UAB. His research interests include data compression, with a focus on task-oriented coding of visual contents, and compression standards. He is an active contributor and a Reviewer in research areas of knowledge.